

**Computation of inclined magnetic field, thermophoresis and Brownian motion effects on mixed convective electroconductive nanofluid flow in a rectangular porous enclosure with adiabatic walls and hot slits**

A. Sumithra<sup>1</sup>

<sup>1</sup>*Department of Mathematics, School of Advanced Sciences  
Vellore Institute of Technology, Vellore 632014, India*

R. Sivaraaj<sup>1, 2, 3 \*</sup>

<sup>1</sup>*Department of Mathematics, School of Advanced Sciences  
Vellore Institute of Technology, Vellore 632014, India*

<sup>2</sup>*Department of Mathematical Sciences, United Arab Emirates University  
Al Ain, United Arab Emirates  
Department of Mathematics*

<sup>3</sup>*Dr B. R. Ambedkar National Institute of Technology Jalandhar  
Punjab 144027, India  
sivaraaj.kpm@gmail.com*

V. Ramachandra Prasad<sup>1</sup>

<sup>1</sup>*Department of Mathematics, School of Advanced Sciences  
Vellore Institute of Technology, Vellore 632014, India*

O. Anwar Bég<sup>4</sup>

<sup>4</sup>*Multi-Physical Engineering Sciences Group  
Aeronautical and Mechanical Engineering Department  
School of Science, Engineering and Environment, University of Salford  
Manchester M54WT, UK*

Ho-Hon Leung<sup>2</sup>

<sup>2</sup>*Department of Mathematical Sciences  
United Arab Emirates University, Al Ain, United Arab Emirates*

Firuz Kamalov<sup>5</sup>

<sup>5</sup>*Faculty of Engineering, Canadian University Dubai  
Dubai, United Arab Emirates*

S. Kuharat<sup>4</sup>

<sup>4</sup>*Multi-Physical Engineering Sciences Group  
Aeronautical and Mechanical Engineering Department  
School of Science, Engineering and Environment, University of Salford*

*Manchester M54WT, UK*

B. Rushi Kumar<sup>1</sup>

<sup>1</sup>*Department of Mathematics, School of Advanced Sciences  
Vellore Institute of Technology, Vellore 632014, India*

Received Day Month Year

Revised Day Month Year

The present analysis theoretically investigates the transport phenomena of mixed convection flows in an enclosure of rectangular geometry saturated with a permeable medium filled with an electrically conducting nanofluid. An inclined magnetic field is taken into consideration. Buongiorno's model is utilized to characterize the nanofluid. The enclosure has adiabatic walls and hot slits. A uniform cold temperature is maintained at the enclosure's lower and upper walls. The enclosure's vertical walls are thermally insulated with hot slits at the center of the walls. This kind of analysis on mixed convective, electrically conducting nanofluid flows in enclosures finds applications in smart nanomaterial processing systems and hybrid electromagnetic nanofluid fuel cells. The Marker-And-Cell (MAC) method is utilized to solve the transformed non-dimension system of governing equations subject to the fitted boundary conditions. The effects of key physical parameters on streamlines, isotherms, iso-concentrations contour plots, and the heat transmission rate are examined. The simulations demonstrate that the Richardson number has a predominant impact on the thermo-solutal features of nanofluid flow in the rectangular enclosure. Variations in magnetic field and buoyancy ratio parameters exert a notable influence on the iso-concentrations and isotherms. An increase in the Darcy number values exhibits a tendency to magnify the local heat transfer rate. Higher Grashof number values reduce the local Nusselt number profiles. The effect of porous parameter is significant in the streamlines, isotherms, and iso-concentrations. Thus, the porous medium can significantly control the transport phenomena in the enclosure. The concentration, temperature, and velocity contours are strongly modified by the variations in the Grashof number.

*Keywords:* Nanofluid; porous medium; inclined magnetic field; mixed convection; Buongiorno's mathematical model; MAC method.

## Nomenclature

$x, y$	dimensional Cartesian coordinates [ $m$ ]
$K$	permeability of the porous medium [ $m^2$ ]
$H$	Height of the cavity [ $m$ ]
$B_0$	magnetic field strength [ $kg\ s^{-2}\ A^{-1}$ ]
$g$	acceleration due to gravity [ $m\ s^{-2}$ ]
$p$	dimensional pressure [ $Pa$ ]
$D_T$	thermophoresis diffusion coefficient [ $m^2\ s^{-1}$ ]
$U_0$	constant reference velocity [ $m\ s^{-1}$ ]
$C$	dimensional concentration of the fluid [ $kg\ m^{-3}$ ]
$T$	dimensional temperature of the fluid [ $K$ ]
$C_c$	low concentration [ $kg\ m^{-3}$ ]
$T_c$	temperature of the cold wall [ $K$ ]
$U, V$	dimensionless velocities along X and Y directions [-]
$C_h$	high concentration [ $kg\ m^{-3}$ ]
$L$	Length of the cavity [ $m$ ]
$T_h$	temperature of the hot wall [ $K$ ]
$u, v$	dimensional velocity components in $x, y$ directions [ $m\ s^{-1}$ ]
$Re$	Reynolds number [-]
$t^*$	dimensional time [ $s$ ]
$Gr$	Grashof number [-]
$P$	dimensionless pressure [-]
$Nu$	local Nusselt number [-]
$Nr$	buoyancy ratio parameter [-]
$Da$	Darcy number [-]
$X, Y$	dimensionless Cartesian coordinate system [-]
$Pr$	Prandtl number [-]
$N_T$	thermophoresis parameter [-]
$Ha$	Hartmann number [-]
$N_B$	Brownian motion parameter [-]
$Ri$	Richardson number [-]
$Sc$	Schmidt number [-]

**Greek symbols**

$\beta_f$	thermal expansion coefficient [ $K^{-1}$ ]
$\phi$	dimensionless concentration [-]
$\theta$	dimensionless temperature [-]
$\sigma_f$	electrical conductivity of the fluid [ $S m^{-1}$ ]
$\mu_f$	dynamic viscosity of the fluid [ $kg m^{-2} s^{-1}$ ]
$\nu_f$	kinematic viscosity of the fluid [ $m^2 s^{-1}$ ]
$\alpha_f$	thermal diffusivity of the fluid [ $m^2 s^{-1}$ ]
$\rho_f$	density of the fluid [ $kg m^{-3}$ ]
$\Phi$	magnetic field inclination angle [ $rad$ ]
$\rho_p$	density of the nanoparticle [ $kg m^{-3}$ ]

**1. Introduction**

Choi and Eastman<sup>1</sup> invented the term nanofluid. Nanofluid is a colloidal suspension that contains nanoparticles with high thermophysical properties. Nanofluids contain base fluids such as petrolatum, ethylene glycol, water, engine oil, and 1 to 100 nm-sized nanoparticles with high thermal conductivity. Popular nanoparticles include *Cu*, *Al*, *Ag*, *Al<sub>2</sub>O<sub>3</sub>*, *TiO<sub>2</sub>*. Nanoparticles with high thermal resistivity are dispersed into base fluids with minimum thermal conductivity to boost the thermal resistivity of the base fluids. In current years, nanofluid has been deployed extensively in many engineering systems. They have been demonstrated to achieve successful performance in heat transfer enhancement in diverse technologies including heat exchangers, nuclear reactor cooling, hydronic heating, and cooling systems in buildings, materials fabrication processes, electronic cooling systems, and hybrid fuel cells. Over the last few decades, heat transmission of nanofluids contained in a variety of cavity geometries (enclosures) under different thermal conditions has been scrutinized by many researchers. Mostafazadeh et al.<sup>2</sup> studied the natural convection of nanofluid in a vertical channel. They concluded that the increasing solid nanoparticle volume fraction results in lowering the velocity contour elevations. Basdar et al.<sup>3</sup> investigated the heat transmission of nanofluid inside a wavy microchannel. They found that the rising values of the nanoparticle volume fraction enhance the local heat transmission rate. Laidoudi et al.<sup>4</sup> studied the motion of a hybrid nanofluid trapped inside a three-dimensional container. The heat transfer enhances for rising values of the nanoparticle volume fraction. Jirawattanapanit et al.<sup>5</sup> analyzed the melting rate enhancement inside a heat Pipe. They concluded that the copper nanoparticle enhances the heat transmission in the interior of the enclosure. Sumithra and Sivaraj<sup>6</sup> described the characteristics of mixed convective nanofluid flow in a rectangular enclosure through numerical computations using the Marker-And-Cell method, noting that nanofluid elucidates higher heat transfer with higher thermophoresis parameter values. Sumithra and Sivaraj<sup>7</sup> studied the mixed convective nanofluid flow over a square enclosure. They concluded that the nanofluid mass transfer enhances for raising values of the thermophoresis parameter.

Shah et al.<sup>8</sup> exploited the thermally enhanced EMHD micropolar nanofluid model flow via a horizontal Riga device. They concluded that raising the thermophoresis parameter increased the nanofluid temperature. Sajjan et al.<sup>9</sup> investigated the 3D flow of nanofluid shape factors inside a rectangular closed zone. They inferred that the volume percentage of nanoparticles lowered the temperature. Zhang et al.<sup>10</sup> investigated the 3D convective hybrid nanofluid flow in a suspension of different temperatures of water. They concluded that the friction factor is higher in normal water compared to water at 10 degree Celsius. Shah et al.<sup>11</sup> investigated unsteady convective nanofluid flow in a rectangular channel. They concluded that increasing the nanoparticle volume fraction improved heat transfer.

Convective flow in permeable (porous) media has gained extensive attention in thermal engineering sciences during the past few decades, owing to diverse applications including thermal energy storage, sensible heat storage beds, insulation of heated bodies, drying processes (wood and food products), filtration processes, hybrid fuel cell designs, and materials fabrication technologies. The porous medium may be sparsely or densely packed. It can be either isotropic (constant permeability) or anisotropic (variable permeability in different directions). Porous media via the presence of solid matrix fibers can be used to regulate momentum and heat transfer characteristics inexpensively. At low velocities, the Darcy model is usually employed. It stipulates that the rate of flow is proportional to the pressure drop across a porous medium. This model is broadly valid for Reynolds numbers up to 10. It quite accurately simulates transport in a single-phase system and introduces a linear drag force (bulk matrix impedance) into the momentum balance equation. As such the Darcy model has been widely utilized in analyzing both Newtonian and non-Newtonian percolation in porous media. Kefayati<sup>12</sup> examined the transport phenomena of power-law fluid within an oblique permeable enclosure and demonstrated that magnifying the porous parameter augments the entropy generation due to viscous drag. Umavathi and Beg<sup>13</sup> studied the double-diffusive convection in a horizontal permeable enclosure loaded with an incompressible non-Newtonian nanoliquid by considering the viscosity and thermal conductivity variations. They used a polar Stokes couple stress model and examined the problem using a nonlinear Fourier series method. They elucidated that a couple stress parameter and the Darcy number arguments the system's stability in both the oscillatory and stationary convection modes. A mathematical model that examines the transport phenomena in an oblique permeable cavity filled with  $Cu/H_2O$ -nanoliquid was noted by Rashad et al.<sup>14</sup>. They reported that the free convection energy transmission mechanism is dominant and heat transmission diminishes for minifying the Rayleigh number values. Aneja et al.<sup>15</sup> described the flow of non-Newtonian fluid in a partially heated permeable enclosure, noting that higher porous parameter values increase the mean Nusselt number. The EMHD nanofluid flows past a Riga pattern in a Darcy-Forchheimer permeable medium, as examined by Rasool et al.<sup>16</sup>. They observed that the resulting frictional factor at the Riga surface was strengthened by

the Darcy-Forchheimer parameter.

When forced convection and natural convection mechanisms occur together, mixed convection arises and all these convections contribute to the transmission of heat. The mixed convection mechanism is considered to be more complex than the other modes of convection due to the combination of buoyancy and shear force. The modeling of forced and free-convection heat transmission within enclosures filled with nanofluids has been the subject of interest to several industries. Mixed convection heat transfer has received much attention in several areas including thermal management, solar collectors, crystal growth, and cooling of electronic systems. There have been many attempts to enhance heat transmission efficiency in several engineering and industrial applications by using a wide range of techniques. In this regard, nanofluids and another complex fluent media have proven very promising. Elshehabe and Ahmed<sup>17</sup> studied the free and forced convection nanoliquid flow in a cavity of lid-driven type. They exhibited that the density of the streamlines in the enclosure decreases with higher buoyancy ratio parameter values. Free and forced convective MHD flow in a cavity of lid-driven type filled with a ferrofluid was taken out by Gibanov et al.<sup>18</sup>. Khan et al.<sup>19</sup> analyzed the influence of radiation on convection flow in a permeable enclosure, observing that the fluid temperature boosts for growing values of the Grashof number.  $Cu - H_2O$  nanoliquid flow in a cavity of lid-driven type in the existence of magnetic field was analyzed by Cho<sup>20</sup>. He noticed that an enhancement in Richardson and Reynolds numbers amplifies the mean Nusselt number. The time-independent natural convective nanofluid flow in a cavity was scrutinized by Hussain and Ahmad<sup>21</sup>. They identified that the average Nusselt number decays for magnifying the bouncy ratio parameter values. Abu-Hamdeh et al.<sup>22</sup> investigated the convection flow in a permeable cavity and concluded that the Grashof number plays a critical role in controlling velocity and thermal fields. Eswaramoorthi et al.<sup>23</sup> studied convective heat and mass transfer in a Riga plate. They discovered that as the Reynolds number rises, so does the creation of entropy.

With the emergence of new smart electro-conductive nanomaterials, the magnetic field effect on the transport phenomena of nanoliquids has attracted widespread consideration. Important areas where such intelligent nano-liquids are being implemented owing to their multi-functionality include novel fuel cells, MAGEV lubrication systems, magnetic solar cell technology, magnetic materials processing, plasma flow control in nuclear power, smart sensors, responsive aerospace systems, and naval coatings. The study of electro-conductive nanofluids requires a combination of the science of magnetohydrodynamics (MHD) and nanofluid mechanics. In many systems either static or oscillating, transverse or oblique (inclined) magnetic fields may be deployed to manipulate magneto-nanofluid behavior. Selimefendigil et al.<sup>24</sup> numerically examined the magnetohydrodynamic mixed convective flow of a nanoliquid within a triangular domain and observed that the average heat transmission can be improved more when raising the inclined magnetic field angle of the upper triangular domain. Bondareva and Sheremet<sup>25</sup> scrutinized the MHD

free-convection melting in a cavity, noting that a significant modification is observed in isotherms, Nusselt number, and isovels with variations in the angle of inclination. Mehmood et al.<sup>26</sup> explored the influence of radiation and oblique magnetic field on mixed convective nanoliquid flow in an enclosure of square type, observing that depletion in the rate of energy transmission is induced with a mount in magnetic field inclination angle. Selimefendigil and Oztop<sup>27</sup> examined the effect of an oblique magnetic field on nanoliquid transport in a cavity containing a curved-shaped conductive partition and concluded that the escalating Hartmann number values diminish the entropy generation. Mansour et al.<sup>28</sup> explored the hydromagnetic flow of non-Newtonian nanoliquid in a cavity of double-lid driven using a local thermal non-equilibrium model with the presence of an oblique magnetic field and noticed that temperature increases according to boost in Hartmann number values. Hussain et al.<sup>29</sup> studied numerically with cubic polynomials to evaluate the impact of oblique magnetic field and fins in a cavity of lid-driven type filled with a magnetized  $Cu - H_2O$  nanoliquid. They observed that the magnetic field applied in the upright direction is more effective on transport phenomena of  $Cu - H_2O$  nanoliquid compared with the inclined angles of the magnetic field. Heat and MHD nanofluid flow over a stretched sheet were studied by Rauf et al.<sup>30</sup>. They found that as the magnetic parameter increased, the stream function decreased.

When the heat transmission coefficient increases beyond pure thermal conduction effects, the traditional pure fluid correlations like the Dittus-Boelters correlation cannot predict the fluid temperature characteristics precisely. In nanofluids, many possible mechanisms have been identified to enhance heat transfer. Buongiorno<sup>31</sup> developed a two-component thermo-solutal model in which he emphasized the following seven slip-mechanisms: thermophoresis, inertia, fluid drainage, Brownian diffusion, diffusion-phoresis, gravity, and the Magnus effect. He concluded that thermophoresis (motion of nanoparticles under a temperature gradient) and Brownian diffusion (chaotic motion of nanoparticles) play an essential part in predicting the transport phenomena of nanofluids. This model has the advantage over other nanofluid formulations in that it includes a species diffusion equation which can be used to compute the nanoparticle concentration (volume fraction) variation and has been implemented in many respected studies. Sheremet and Pop<sup>32</sup> summarized the steady laminar mixed convective nanoliquid flow in a lid-driven cavity using the Buongiorno model and noticed that nanoparticle mass transfer enhances for magnifying the Brownian motion and thermophoresis parameters. Kefayati and Sidik<sup>33</sup> computationally examined the entropy generation on free convective nanofluid flow in an inclined enclosure. He concluded that an augment in Brownian motion and thermophoresis parameters significantly diminish the average Bejan number. Time-dependent MHD nanoliquid flow via a stretching surface with thermophoresis and Brownian motion were scrutinized by Kumaran et al.<sup>34</sup> by adopting the Buongiorno model. They noticed that the Sherwood and Nusselt numbers magnify for enhancing the Brownian motion parameter values. Time-dependent nanoliquid flow via a plate and cone with thermophoresis and Brownian motion were analyzed by

Basha et al.<sup>35</sup> and they observed that the Brownian motion and thermophoresis have similar effects on energy distribution and have opposite behaviors on concentration distribution. Wang et al.<sup>36</sup> adapted the Buongiorno model to scrutinize the free convective nanofluid flow in an enclosure and inferred that the impact of thermophoretic diffusion is stronger than Brownian motion. The natural convective flow of nanoliquids inside a cavity with conjugate solid triangular blocks were analyzed by Zadeh et al.<sup>37</sup> and came to the conclusion that as the thermal conductivity ratio decreases, the concentration of nanoparticles along the triangular walls considerably increases. Reddy and Sreedevi<sup>38</sup> investigated the Buongiorno nanofluid dynamics within a square enclosure and determined that heat transfer augments for enhancing the thermophoresis parameter values. Beg et al.<sup>39</sup> theoretically investigated the impact of thermal radiation and variable thermophysical properties on magnetic pseudoplastic nanofluid flow via a circular cylinder and they demonstrated that the heat transmission augments for amplifying the thermophoresis parameter. Basha et al.<sup>40</sup> predicted the forced convective Falkner-Skan slip flow of a viscoelastic nanofluid in the occurrence of variable Prandtl number and temperature-dependent viscosity, noting that fluid temperature rises for magnifying the slip parameter and thermophoresis parameter values. Basha and Sivaraj<sup>41</sup> investigated the Casson nanofluid stagnation point flow via a wedge and they inferred that the Brownian motion and thermophoresis motion parameters attain the same critical point values on the heat transmission distribution. Further studies deploying the Buongiorno model in electromagnetic nanofluid transport include Prakash et al.<sup>42</sup> (on rotating coating systems), Shamshuddin et al.<sup>43</sup> (who considered the impact of a chemical reaction), and Umavathi et al.<sup>44</sup> (who studied magneto-nano-tribological squeezing flows). All these studies confirmed the substantial effect of thermophoresis and Brownian motion on both concentration and thermal fields.

The impact of magnetic field effect on mixed convective nanofluid flow within a rectangular permeable cavity is reported in the literature. To the most promising of the author's knowledge, to date, no work has been noted in the scientific literature to investigate the inclined (oblique) magnetic field effect on mixed convective nanofluid flow within a rectangular permeable cavity with adiabatic walls and hot slits. Therefore, the present investigation intent to examine this study. The Buongiorno model is adopted. A uniform cold temperature is kept in the lower and upper walls of the enclosure. The enclosure's Vertical walls are thermally insulated with hot slits at the center of the walls. The equations that represent the present model are solved by utilizing the Marker and Cell finite difference scheme<sup>45,46</sup> and the numerical results for streamlines, isotherms, iso-concentrations, and the local heat transmission rate are illustrated graphically. This study intends to answer the following research questions: 1. What kind of convection has more influence on the interior of the cavity? 2. What is the impact of porous medium on nanofluid flow inside the enclosure? 3. What is the impact of buoyancy effect on fluid flow? 4. How do the variations

in the inclined magnetic field affect the nanofluid case? The present simulations are relevant to hybrid magnetic fuel cells exploiting nanofluids<sup>47,48,49,50,51</sup> and the importance of nanomaterial on electromagnetic flow processing<sup>52</sup>.

## 2. Mathematical formulation

The unsteady, laminar, mixed convective electro-conductive nanofluid flow in a saturated isotropic, homogenous permeable medium contained within a rectangular cavity with adiabatic walls and hot slits is considered. Figure. 1 illustrates the flow configuration of the problem along with no-slip thermal boundary conditions. The proposed model makes certain implicit assumptions:

- (1) The cavity's vertical walls are thermally insulated with hot slits at the middle of the walls.
- (2) The cavity's top and bottom walls remain with cold temperature.
- (3) The gravity acts along the normal direction.
- (4) The density variation is characterized through buoyancy term by adopting the Boussinesq approximation.
- (5) The effect of an oblique magnetic field with the inclination angle  $\Phi$  (to the horizontal) is considered within the flow domain.
- (6) The Buongiorno two-component model is utilized to characterize the nanofluid and hence species diffusion, thermophoresis, and Brownian motion effects are included in this study.

Based on these assumptions, the governing equations in a two-dimensional Cartesian coordinate system are represented as follows<sup>12,17,21,46,54</sup>:

$$\frac{\partial u}{\partial x} + \frac{\partial v}{\partial y} = 0, \quad (1)$$

$$\rho_f \left( \frac{\partial u}{\partial t^*} + u \frac{\partial u}{\partial x} + v \frac{\partial u}{\partial y} \right) = -\frac{\partial p}{\partial x} + \mu_f \left( \frac{\partial^2 u}{\partial x^2} + \frac{\partial^2 u}{\partial y^2} \right) - \frac{\mu_f}{K} u + \sigma_f B_0^2 (v \sin \Phi \cos \Phi - u \sin^2 \Phi), \quad (2)$$

$$\rho_f \left( \frac{\partial v}{\partial t^*} + u \frac{\partial v}{\partial x} + v \frac{\partial v}{\partial y} \right) = -\frac{\partial p}{\partial y} + \mu_f \left( \frac{\partial^2 v}{\partial x^2} + \frac{\partial^2 v}{\partial y^2} \right) - \frac{\mu_f}{K} v + \sigma_f B_0^2 (u \sin \Phi \cos \Phi - v \cos^2 \Phi) + [(1 - C_c) \rho_f (T - T_c) \beta_f - (C - C_c) (\rho_p - \rho_f)] g, \quad (3)$$

$$\frac{\partial T}{\partial t^*} + u \frac{\partial T}{\partial x} + v \frac{\partial T}{\partial y} = \alpha_f \left( \frac{\partial^2 T}{\partial x^2} + \frac{\partial^2 T}{\partial y^2} \right) + \tau \left[ D_B \left( \frac{\partial T}{\partial x} \frac{\partial C}{\partial x} + \frac{\partial C}{\partial y} \frac{\partial T}{\partial y} \right) + \frac{D_T}{T_c} \left( \left( \frac{\partial T}{\partial x} \right)^2 + \left( \frac{\partial T}{\partial y} \right)^2 \right) \right], \quad (4)$$

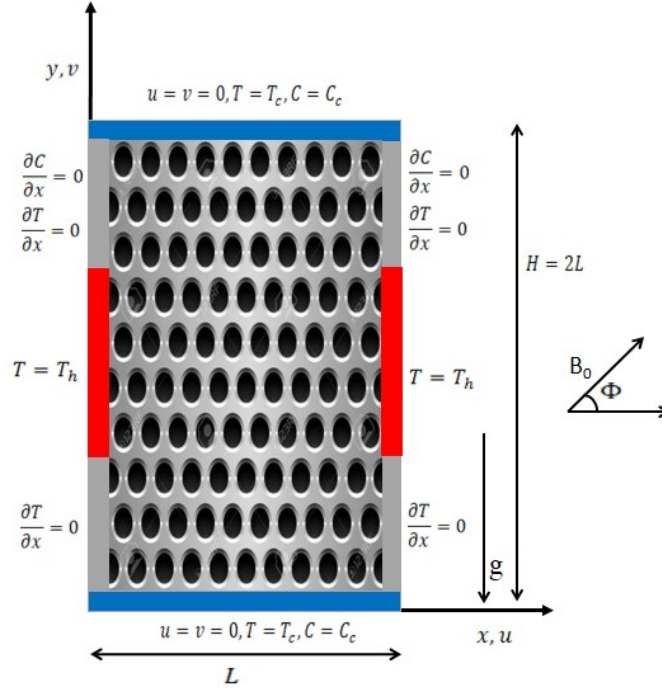


Fig. 1. Flow configuration.

$$\frac{\partial C}{\partial t^*} + u \frac{\partial C}{\partial x} + v \frac{\partial C}{\partial y} = D_B \left( \frac{\partial^2 C}{\partial x^2} + \frac{\partial^2 C}{\partial y^2} \right) + \frac{D_T}{T_c} \left( \frac{\partial^2 T}{\partial x^2} + \frac{\partial^2 T}{\partial y^2} \right). \quad (5)$$

The dimensional initial and boundary conditions of the problem are as follows:

$$t^* \leq 0, \quad 0 \leq x \leq L, \quad 0 \leq y \leq 2L : \quad u = v = 0, \quad T = T_c, \quad C = C_c. \quad (6)$$

On the top wall of the domain:

$$t^* > 0, \quad y = 2L, \quad 0 < x < L : \quad u = v = 0, \quad T = T_c, \quad C = C_c. \quad (7)$$

On the bottom wall of the domain:

$$t^* > 0, \quad y = 0, \quad 0 < x < L : \quad u = v = 0, \quad T = T_c, \quad C = C_c. \quad (8)$$

On the left wall of the domain:

$$\begin{aligned}
 t^* > 0, \quad x = 0, \quad 0 < y < 2L: \quad u = v = 0, \quad \frac{\partial C}{\partial x} = 0, \\
 \frac{\partial T}{\partial x} = 0 \quad \text{for} \quad 0 < y < \frac{L}{2}, \\
 T = T_h \quad \text{for} \quad \frac{L}{2} < y < \frac{3L}{2}, \\
 \frac{\partial T}{\partial x} = 0 \quad \text{for} \quad \frac{3L}{2} < y < 2L.
 \end{aligned} \tag{9}$$

On the right wall of the domain:

$$\begin{aligned}
 t^* > 0, \quad x = L, \quad 0 < y < 2L: \quad u = v = 0, \quad \frac{\partial C}{\partial x} = 0, \\
 \frac{\partial T}{\partial x} = 0 \quad \text{for} \quad 0 < y < \frac{L}{2}, \\
 T = T_h \quad \text{for} \quad \frac{L}{2} < y < \frac{3L}{2}, \\
 \frac{\partial T}{\partial x} = 0 \quad \text{for} \quad \frac{3L}{2} < y < 2L.
 \end{aligned} \tag{10}$$

To remove the dimensions of the boundary value problem defined by ‘‘Eqs. (1- 10)’’, the following non-dimension parameters are invoked:

$$\begin{aligned}
 U = \frac{u}{U_0}, \quad Y = \frac{y}{L}, \quad t = \frac{t^* U_0}{L}, \quad X = \frac{x}{L}, \quad V = \frac{v}{U_0}, \quad P = \frac{p}{\rho_f U_0^2}, \\
 \theta = \frac{T - T_c}{T_h - T_c}, \quad \phi = \frac{C - C_c}{C_h - C_c}, \quad Re = \frac{U_0 L}{\nu_f}, \quad Pr = \frac{\nu_f}{\alpha_f}, \quad \nu_f = \frac{\mu_f}{\rho_f}, \\
 N_T = \frac{\tau D_T (T_h - T_c)}{T_c \alpha_f}, \quad Sc = \frac{\nu_f}{D_B}, \quad N_B = \frac{\tau D_B (C_h - C_c)}{\alpha_f}, \\
 Ha = B_0 L \sqrt{\frac{\sigma_f}{\mu_f}}, \quad Da = \frac{K}{L^2}, \quad Gr = \frac{g \beta_f (1 - C_c) (T_h - T_c) L^3}{\nu_f^2}, \\
 Ri = \frac{Gr}{Re^2}, \quad Nr = \frac{(C_h - C_c) (\rho_p - \rho_f)}{(1 - C_c) \rho_f (T_h - T_c) \beta_f}.
 \end{aligned} \tag{11}$$

Using ‘‘Eq. (10)’’ in ‘‘Eqs. (1- 5)’’, the transformed non-dimension governing equations emerge as:

$$\frac{\partial U}{\partial X} + \frac{\partial V}{\partial Y} = 0, \tag{12}$$

$$\begin{aligned}
 \frac{\partial U}{\partial t} + U \frac{\partial U}{\partial X} + V \frac{\partial U}{\partial Y} = -\frac{\partial P}{\partial X} + \frac{1}{Re} \left( \frac{\partial^2 U}{\partial X^2} + \frac{\partial^2 U}{\partial Y^2} \right) - \frac{1}{Re Da} U \\
 + \frac{Ha^2}{Re} (V \sin \Phi \cos \Phi - U \sin^2 \Phi),
 \end{aligned} \tag{13}$$

12 *A. Sumithra, V. R. Prasad, R. Sivaraj, Ho-Hon Leung, O. A. Béq & Firuz Kamalov, S. Kuharat, B. Rushi Kumar*

$$\begin{aligned} \frac{\partial V}{\partial t} + U \frac{\partial V}{\partial X} + V \frac{\partial V}{\partial Y} = -\frac{\partial P}{\partial Y} + \frac{1}{Re} \left( \frac{\partial^2 V}{\partial X^2} + \frac{\partial^2 V}{\partial Y^2} \right) - \frac{1}{Re Da} V + Ri (\theta - Nr \phi) \\ + \frac{Ha^2}{Re} (U \sin \Phi \cos \Phi - V \cos^2 \Phi), \end{aligned} \quad (14)$$

$$\begin{aligned} \frac{\partial \theta}{\partial t} + U \frac{\partial \theta}{\partial X} + V \frac{\partial \theta}{\partial Y} = \frac{1}{Re Pr} \left( \frac{\partial^2 \theta}{\partial X^2} + \frac{\partial^2 \theta}{\partial Y^2} \right) \\ + \frac{N_B}{Re Pr} \left[ \frac{\partial \theta}{\partial X} \frac{\partial \phi}{\partial X} + \frac{\partial \theta}{\partial Y} \frac{\partial \phi}{\partial Y} \right] + \frac{N_T}{Re Pr} \left[ \left( \frac{\partial \theta}{\partial X} \right)^2 + \left( \frac{\partial \theta}{\partial Y} \right)^2 \right], \end{aligned} \quad (15)$$

$$\frac{\partial \phi}{\partial t} + U \frac{\partial \phi}{\partial X} + V \frac{\partial \phi}{\partial Y} = \frac{1}{Sc Re} \left[ \left( \frac{\partial^2 \phi}{\partial X^2} + \frac{\partial^2 \phi}{\partial Y^2} \right) + \frac{N_T}{N_B} \left( \frac{\partial^2 \theta}{\partial X^2} + \frac{\partial^2 \theta}{\partial Y^2} \right) \right]. \quad (16)$$

The transformed dimensionless initial-boundary conditions are written as follows:

$$t \leq 0, \quad 0 \leq X \leq 1, \quad 0 \leq Y \leq 2: \quad U = V = 0, \quad \theta = 0, \quad \phi = 0. \quad (17)$$

On the top wall of the domain:

$$t > 0, \quad Y = 2, \quad 0 < X < 1: \quad U = V = 0, \quad \theta = 0, \quad \phi = 0. \quad (18)$$

On the bottom wall of the domain:

$$t > 0, \quad Y = 0, \quad 0 < X < 1: \quad U = V = 0, \quad \theta = 0, \quad \phi = 0. \quad (19)$$

On the left wall of the domain

$$\begin{aligned} t > 0, \quad X = 0, \quad 0 < Y < 2: \quad U = V = 0, \quad \frac{\partial \phi}{\partial X} = 0, \\ \frac{\partial \theta}{\partial X} = 0 \quad \text{for} \quad 0 < Y < \frac{1}{2}, \\ \theta = 1 \quad \text{for} \quad \frac{1}{2} < Y < \frac{3}{2}, \\ \frac{\partial \theta}{\partial X} = 0 \quad \text{for} \quad \frac{3}{2} < Y < 2. \end{aligned} \quad (20)$$

On the right wall of the domain:

$$\begin{aligned} t > 0, \quad X = 1, \quad 0 < Y < 2: \quad U = V = 0, \quad \frac{\partial \phi}{\partial X} = 0, \\ \frac{\partial \theta}{\partial X} = 0 \quad \text{for} \quad 0 < Y < \frac{1}{2}, \\ \theta = 1 \quad \text{for} \quad \frac{1}{2} < Y < \frac{3}{2}, \\ \frac{\partial \theta}{\partial X} = 0 \quad \text{for} \quad \frac{3}{2} < Y < 2. \end{aligned} \quad (21)$$

The local Nusselt number ( $Nu$ ) is one of the most important physical quantities in cavity flows. It elucidates the relative influence of convection energy transfer to

conduction energy transmission and also quantifies the heat transmission rate to a boundary. It is defined as:

$$Nu = - \left( \frac{\partial \theta}{\partial Y} \right)_{Y=0}. \quad (22)$$

### 3. MAC solution and validation

The non-dimensionalized PDEs, ( 12- 16) under the boundary conditions ( 17- 21) are solved by MAC scheme. The pressure distribution is determined by utilizing the equation of mass ( 12). The numerical results are calculated in terms of momentum components ( $U, V$ ). It is to be noted that the examination of viscosity is not required to obtain the numerical stability of the MAC approach. Cell boundaries have been identified with half-integer values by utilizing the finite difference method. The numerical discretization of the governing equations is described in this section. The discretization of  $X$  and  $Y$ -momentum equation is as follows:

$$U^{n+1} = U^n + dt \left[ - \left( U \frac{\partial U}{\partial X} + V \frac{\partial U}{\partial Y} \right) + \alpha_1 \left( \frac{\partial^2 U}{\partial X^2} + \frac{\partial^2 U}{\partial Y^2} \right) - \alpha_2 U \right] + dt \left[ \alpha_3 (V \sin \Phi \cos \Phi - U \sin^2 \Phi) \right]. \quad (23)$$

$$V^{n+1} = V^n + dt \left[ - \left( U \frac{\partial V}{\partial X} + V \frac{\partial V}{\partial Y} \right) + \alpha_1 \left( \frac{\partial^2 V}{\partial X^2} + \frac{\partial^2 V}{\partial Y^2} \right) - \alpha_2 V \right] + dt \left[ \alpha_3 (U \sin \Phi \cos \Phi - V \cos^2 \Phi) + \alpha_4 (\theta - \alpha_5 \phi) \right]. \quad (24)$$

Here:

$$\alpha_1 = \frac{1}{Re}, \quad \alpha_2 = \frac{1}{Re Da}, \quad \alpha_3 = \frac{Ha^2}{Re}, \quad \alpha_4 = Ri, \quad \alpha_5 = Nr. \quad (25)$$

The discretized temperature equation can be used to calculate  $\theta$  at the next time level ( $\theta^{n+1}$ ) using the following algorithm:

$$\theta^{n+1} = \theta^n + dt \left[ - \left( U \frac{\partial \theta}{\partial X} + V \frac{\partial \theta}{\partial Y} \right) + \chi_1 \left( \frac{\partial^2 \theta}{\partial X^2} + V \frac{\partial^2 \theta}{\partial Y^2} \right) \right] + dt \left[ \chi_2 \left( \frac{\partial \theta}{\partial X} \frac{\partial \phi}{\partial X} + \frac{\partial \theta}{\partial Y} \frac{\partial \phi}{\partial Y} \right) + \chi_3 \left( \left( \frac{\partial \theta}{\partial X} \right)^2 + \left( \frac{\partial \theta}{\partial Y} \right)^2 \right) \right]. \quad (26)$$

Here:

$$\chi_1 = \frac{1}{Re Pr}, \quad \chi_2 = \frac{N_B}{Re Pr}, \quad \chi_3 = \frac{N_T}{Re Pr}. \quad (27)$$

The following discretized concentration equation can be used to calculate  $\phi$  at the next time level ( $\phi^{n+1}$ ) using the following algorithm:

$$\phi^{n+1} = \phi^n + dt \left[ - \left( U \frac{\partial \phi}{\partial X} + V \frac{\partial \phi}{\partial Y} \right) + \zeta_1 \left( \frac{\partial^2 \phi}{\partial X^2} + \frac{\partial^2 \phi}{\partial Y^2} \right) + \zeta_2 \left( \frac{\partial^2 \theta}{\partial X^2} + \frac{\partial^2 \theta}{\partial Y^2} \right) \right] \quad (28)$$

Here:

$$\zeta_1 = \frac{1}{Sc Re}, \quad \zeta_2 = \frac{N_T}{Sc Re N_B}. \quad (29)$$

In each iteration, an incremental step  $dt$  is considered in time until the final time  $t = 1$  is reached.

**Result and discussion:**

This section elucidates the influence of the pertinent parameter values including the buoyancy ratio parameter ( $Nr$ ), the Darcy parameter ( $Da$ ), the Grashof number ( $Gr$ ), the Richardson number ( $Ri$ ), the Schmidt number ( $Sc$ ), the thermophoresis parameter ( $N_T$ ), the Brownian motion parameter ( $N_B$ ), the Prandtl number ( $Pr$ ), and the Reynolds number ( $Re$ ) on momentum and thermo-solutal transport characteristics. The outcomes are elucidated via streamlines, isotherms, and iso-concentrations. Table 1 summarizes the Average Nusselt number values obtained by Wan et al.<sup>53</sup>, Devi et al.<sup>55</sup>, and the present MAC computations. The result computed by adopting the MAC method agree with the literature.

Pertinent parameter	Wan et al. [53]	Devi et al. [55]	MAC Present result
$Ra = 10^3$	1.117	-	1.1184
$Ra = 10^4$	2.254	2.2526	2.2521
$Ra = 10^5$	4.598	4.5907	4.5537

Figure 2 demonstrates that in the nonexistence of a permeable medium, inclined magnetic field, Brownian motion, and thermophoresis effects, the present outcomes coincide exactly based on the outcomes stated by Khan et al.<sup>19</sup>. This confirms the accuracy of the MAC code deployed in the present analysis. Confidence in all subsequent plots displayed (Figs. 3- 10) is therefore justifiably high. The data prescribed is representative of real hybrid fuel cells and appropriate for materials processing operations<sup>20,45,46</sup>.

Figures 3 (A-C) illustrate the streamlines, isotherms, and iso-concentrations contour plots. It is evident that maximum stream function values are augmented for increasing the Darcy number and hence the streamlines are expanded for a higher Darcy number. It is observed from Fig. 3 (streamlines plot) that the Darcy number values ( $Da = 10^{-3}$ ) result in packing the porous matrix most densely. It is a consequence that the permeability is minimal which results in a constraint in the number of vortex cells and the circulation is restricted to the upper half space of the cavity near the cold top wall region with a stronger intensity in the right vortex cell. There is a very small circulation computed in the mid-region and it is absent near the base wall region. The circulation cells are formed vertically, the primary circulation zone

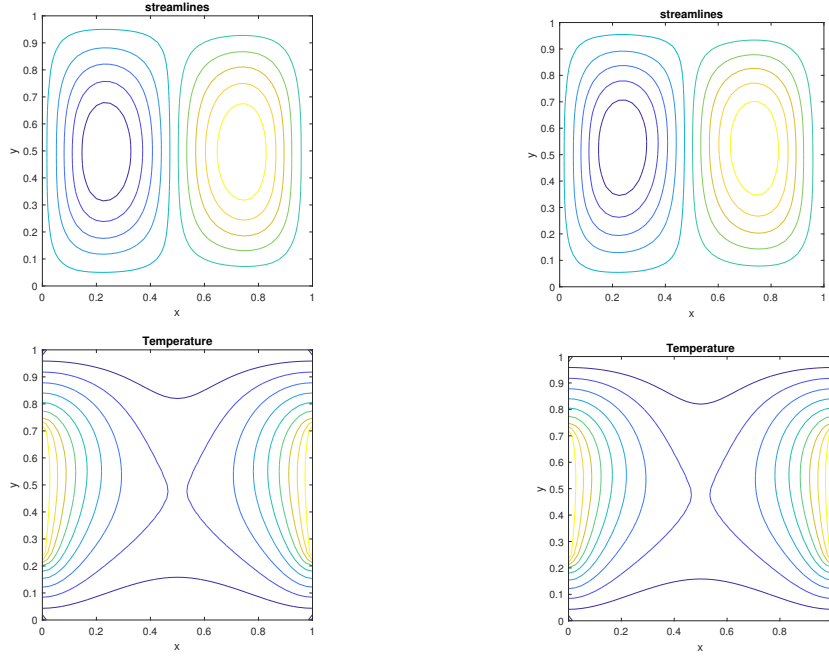


Fig. 2. The comparison contour plots (A) Khan et al.<sup>10</sup> (Left) and (B) Present results (Right) for streamline and isotherms with  $Da = 0.01$ ,  $Gr = 10^4$ ,  $Nr = 1$ ,  $Pr = 0.71$ ,  $Re = 10$ ,  $Ha = 0$ ,  $N_B = 0$ ,  $N_T = 0$ .

is identified at the upper left half of the enclosure and the secondary circulation zone is identified at the upper right half of the enclosure. When the Darcy number is increased ( $Da = 10^{-2}$ ), the primary circulation cells are diminished and new cells appear. Four cells are synthesized in the enclosure and there is a strong skewness in the lower left and upper right cells in the diagonal direction. The lower right vortex cell is elongated in the vertical direction and higher-intensity streamlines are computed. At the maximum permeability ( $Da = 10^{-1}$ ), there is an asymmetric reversal in the distribution of the four vortex cells. In this case, strong skewness is featured in the top left corner and lower right cell, and they are stretched in the opposite diagonal direction. The lower left cell and upper right cell are homogeneous and regular in topology. Clearly, the permeability of the permeable material exerts a considerable effect on the momentum distribution in the cavity. Overall a greater space in the enclosure is occupied although again there is no circulation in the lowermost region near the base wall. The flow is affected via Darcy number by the linear impedance terms,  $-(1/Re Da) U$  in the primary velocity “Eq. (13)” and  $(1/Re Da) V$  in the secondary momentum “Eq. (14)”. Lower Darcy number, owing to the inverse relationship with the Darcian drag terms, leads to a dampening in primary and secondary velocity. This inhibits momentum development and leads to the severely constrained vortex structure observed in Fig. 3 (streamlines plot).

Figure A

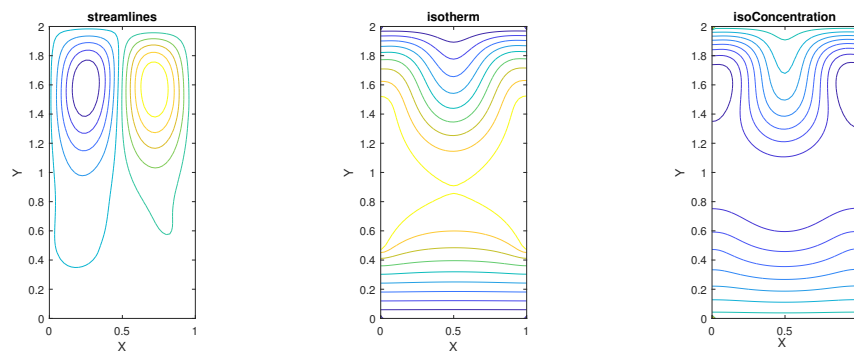


Figure B

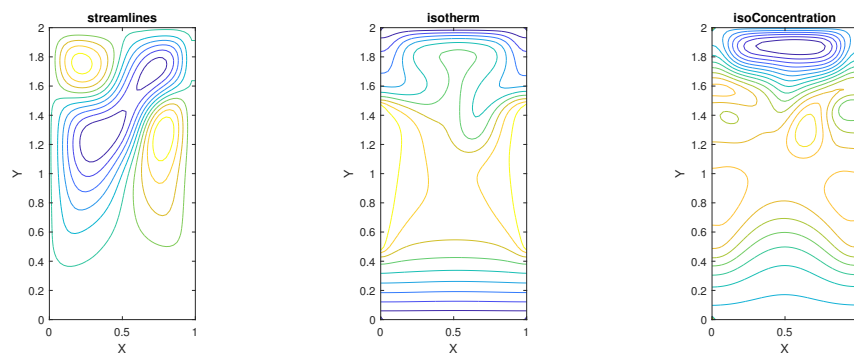


Figure C

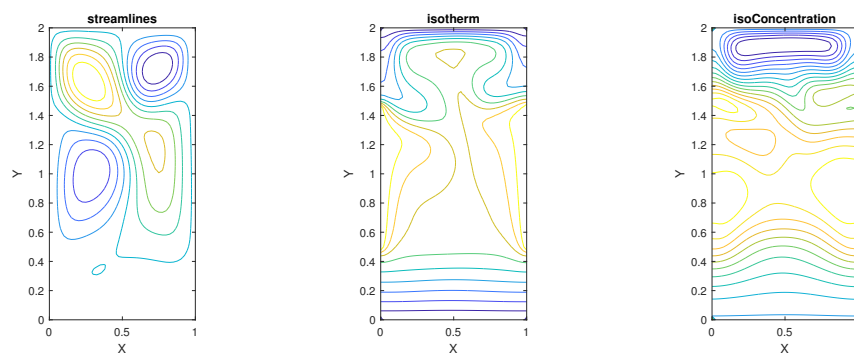


Fig. 3. Streamlines, Isotherms, and Iso-concentrations for (A)  $Da = 10^{-3}$  (B)  $Da = 10^{-2}$  (C)  $Da = 10^{-1}$ , for  $N_T = 0.1$ ,  $Ha = 10$ ,  $N_B = 0.2$ ,  $Gr = 10^4$ ,  $Nr = 1$ ,  $Sc = 0.64$ ,  $Re = 1$ ,  $\Phi = 45$ ,  $Ri = 1$ , and  $Pr = 7$ .

Figure A

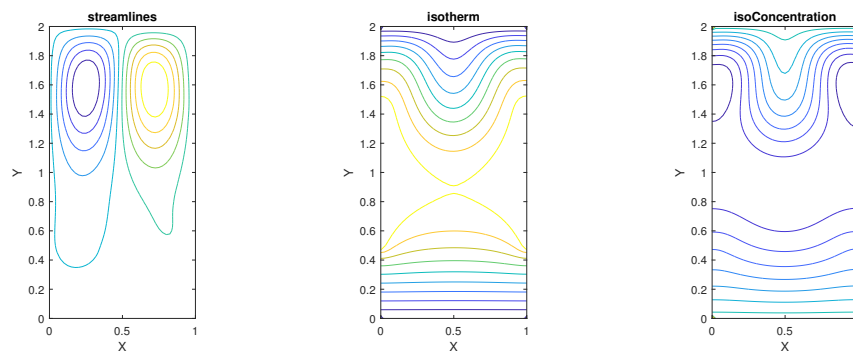


Figure B

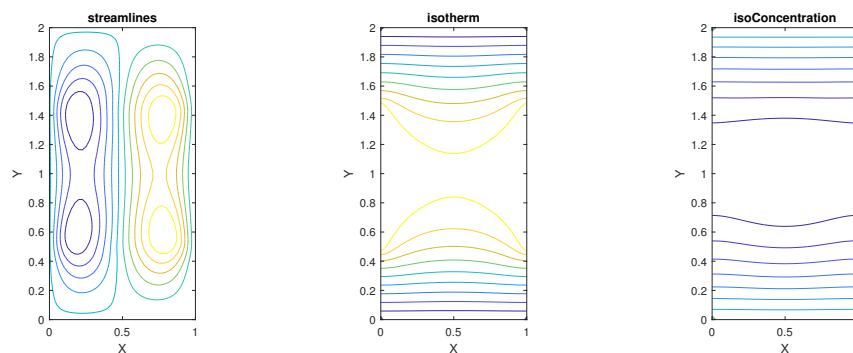


Figure C

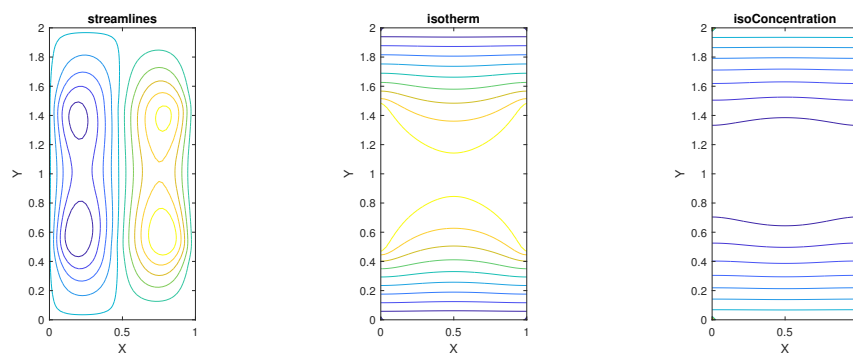


Fig. 4. Streamlines, Isotherms, and Iso-concentrations for (A)  $Gr = 10^2$  (B)  $Gr = 10^3$  (C)  $Gr = 10^4$ , for  $N_T = 0.1$ ,  $Ha = 10$ ,  $N_B = 0.2$ ,  $Da = 0.001$ ,  $Nr = 1$ ,  $Sc = 0.64$ ,  $Re = 1$ ,  $\Phi = 45$ ,  $Ri = 1$ , and  $Pr = 7$ .

Figure A

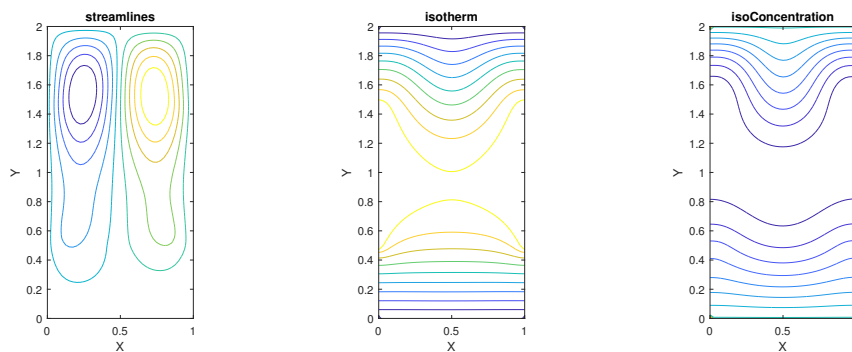


Figure B

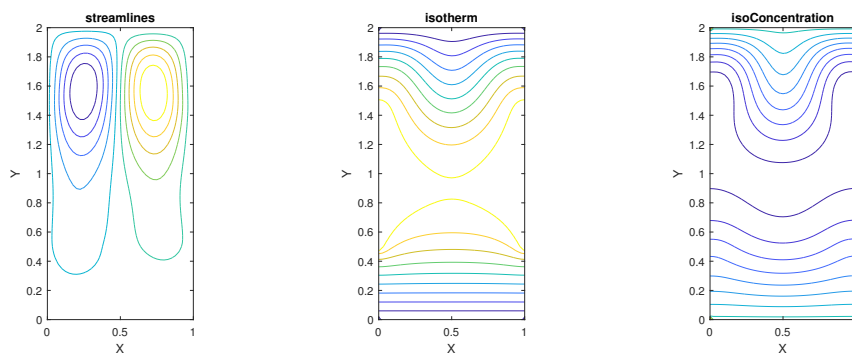


Figure C

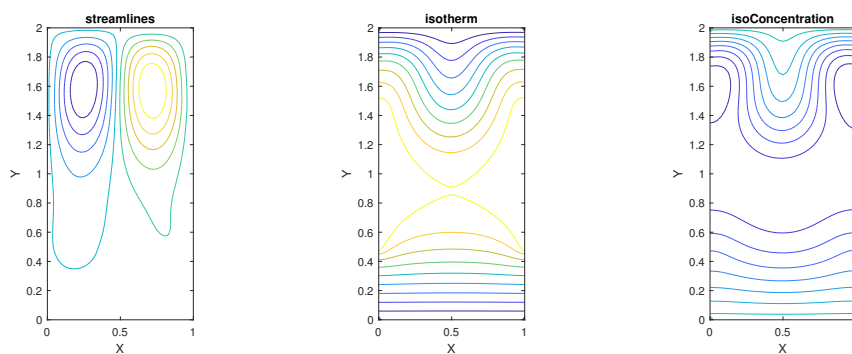


Fig. 5. Streamlines, Isotherms, and Iso-concentrations for (A)  $Nr = 0.1$  (B)  $Nr = 0.5$  (C)  $Nr = 1$ , for  $N_T = 0.1$ ,  $Ha = 10$ ,  $N_B = 0.2$ ,  $Gr = 10^4$ ,  $Da = 0.001$ ,  $Sc = 0.64$ ,  $Re = 1$ ,  $\Phi = 45$ ,  $Ri = 1$ , and  $Pr = 7$ .

Higher Darcy number values produce an acceleration in both the primary and the secondary flow which leads to the appearance of more vortex cells and an expansion

Figure A

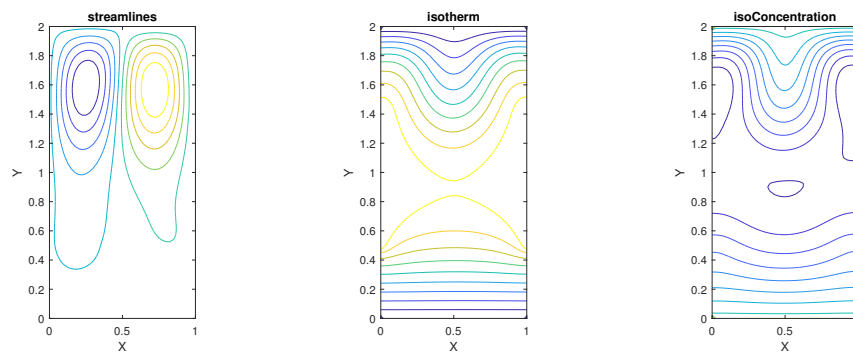


Figure B

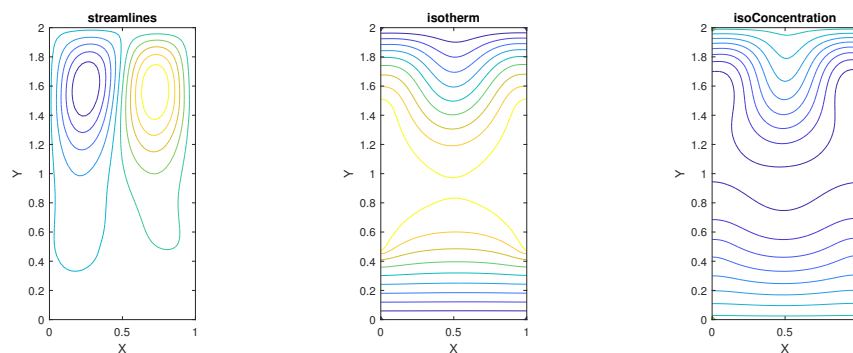


Figure C

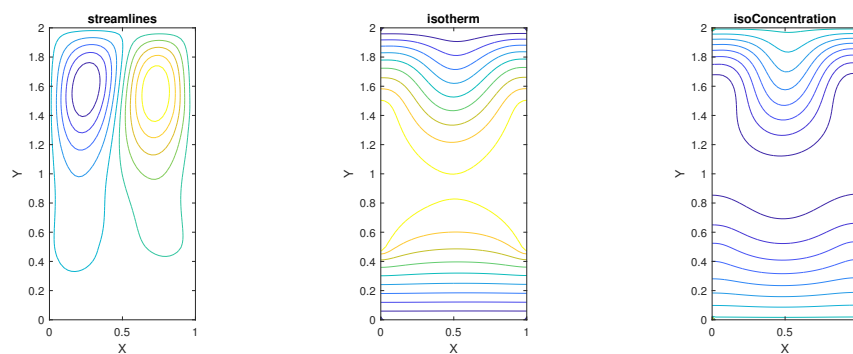


Fig. 6. Streamlines, Isotherms, and Iso-concentrations for (A)  $Ha = 15$  (B)  $Ha = 20$  (C)  $Ha = 25$ , for  $N_T = 0.1$ ,  $Da = 0.001$ ,  $N_B = 0.2$ ,  $Gr = 10^4$ ,  $Nr = 1$ ,  $Sc = 0.64$ ,  $Re = 1$ ,  $\Phi = 45$ ,  $Ri = 1$ , and  $Pr = 7$ .

in the space occupied by the circulation. Figure 3 (isotherms plots) shows that very different patterns are computed at different Darcy numbers for the isotherm

Figure A

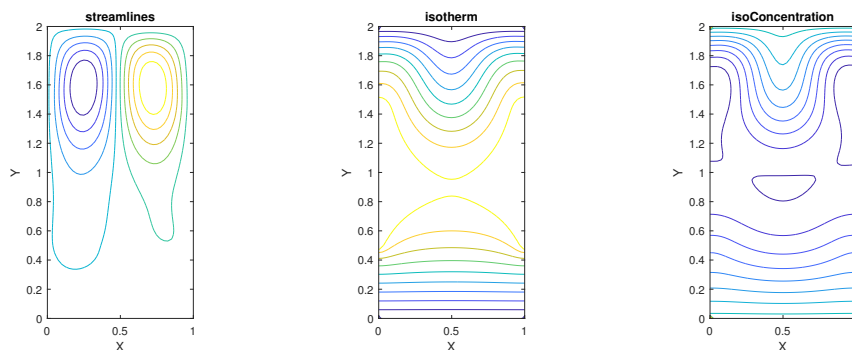


Figure B

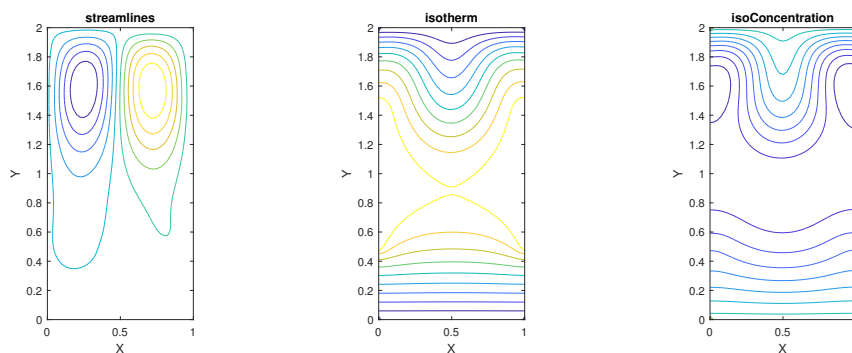


Figure C

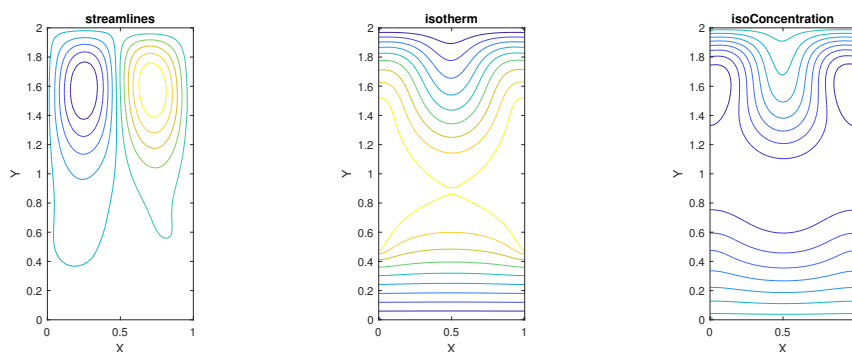


Fig. 7. Streamlines, Isotherms, and Iso-concentrations for (A)  $\Phi = 0$  (B)  $\Phi = \frac{\pi}{4}$  (C)  $\Phi = \frac{\pi}{2}$ , for  $N_T = 0.1$ ,  $Ha = 10$ ,  $N_B = 0.2$ ,  $Gr = 10^4$ ,  $Nr = 1$ ,  $Sc = 0.64$ ,  $Re = 1$ ,  $Da = 0.001$ ,  $Ri = 1$ , and  $Pr = 7$ .

distributions. For  $Da = 10^{-3}$ , isotherms are parallel to the base wall whereas they

Figure A

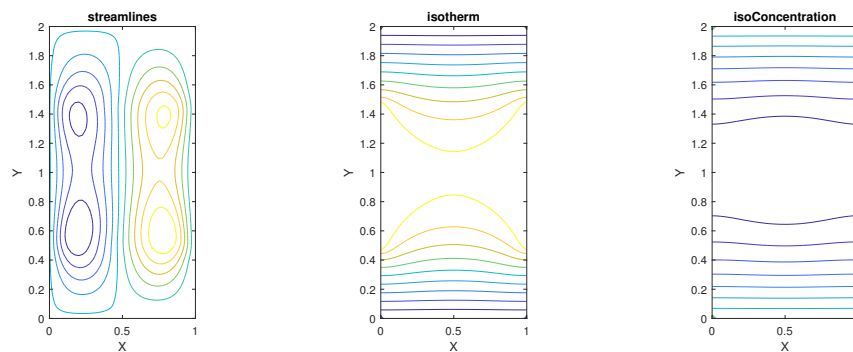


Figure B

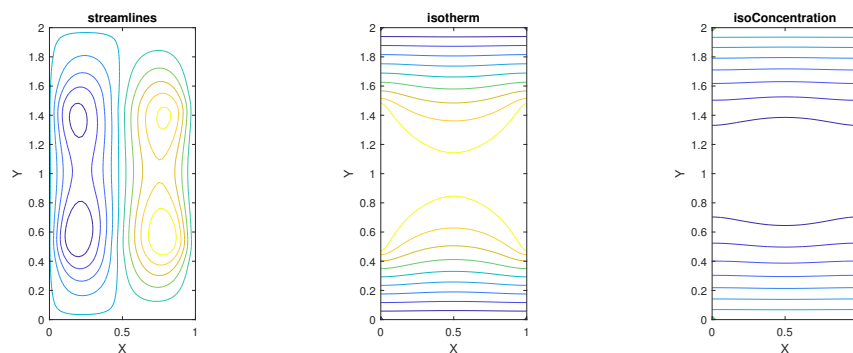


Figure C

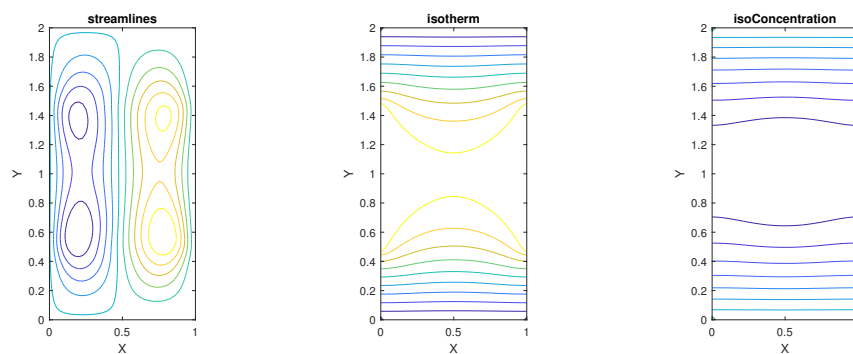


Fig. 8. Streamlines, Isotherms, and Iso-concentrations for (A)  $Ri = 10^{-2}$  (B)  $Ri = 1$  (C)  $Ri = 10^2$ , for  $N_T = 0.1$ ,  $Ha = 10$ ,  $N_B = 0.2$ ,  $Gr = 10^4$ ,  $Nr = 1$ ,  $Sc = 0.64$ ,  $Re = 1$ ,  $\Phi = 45$ ,  $Da = 0.001$ , and  $Pr = 7$ .

are distorted at the upper wall and exhibit a strong parabolic topology deeper into the enclosure. In the central (core) zone, a symmetric isotherm structure is observed

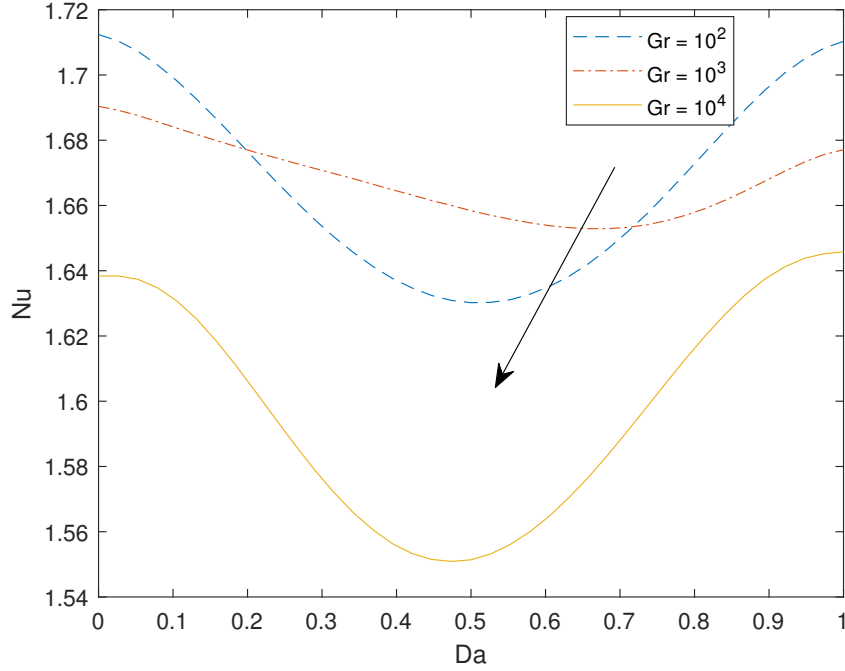


Fig. 9. Rate of heat transfer variation for different  $Gr$  values with  $Da = 0.1$ .

about the vertical centerline, although there is an absence of thermal diffusion near the central sections of the right and left vertical walls. It is important to note that near the two horizontal adiabatic walls, strong thermal conduction is present. With an increment in the Darcy number, lesser solid matrix fibers are present, and this influences thermal conduction within the enclosure. This elucidates the movement of the isotherms between the upper and lower cold wall directions. The heated fluid particle movement is intensified in the upward direction and further observed that an increase in the Darcy number i.e. lower permeability and lower Darcian drag forces strengthen the convection process. The upper nonlinear isotherm patterns become increasingly distorted and an upper central cell near the top wall emerges clearly at a maximum  $Da$  of  $10^{-1}$ . There is pronounced distortion in the isotherms near to the vertical walls and the symmetry is lost. Greater thermal diffusion is achieved in the core zone (central region of the enclosure) and hotter isotherms push more deeply toward the center of the cell which characterizes the mobilization of more intense thermal convection relative to thermal conduction effects. Figure 3 (iso-concentrations plots) indicates that a substantial evolution in iso-concentrations is induced with progressive increment in Darcy number. The central zone of the enclosure exhibits the absence of species diffusion for  $Da = 10^{-3}$ . Only at the upper wall, the nanoparticle diffusion is mobilized and it is symmetrical. Towards the base

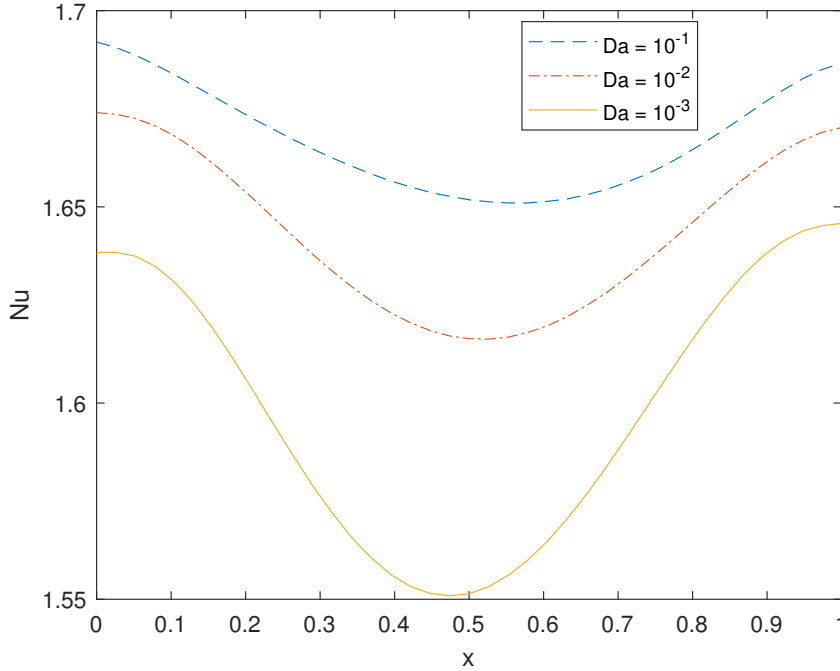


Fig. 10. Rate of heat transfer variations for different  $Da$  values with  $Gr = 10^3$ .

wall, weaker mass diffusion is computed. For magnifying the Darcy number to  $10^{-2}$ , there is a suppression in the iso-concentrations at the upper wall and the expansion of mass diffusion in the core zone. This eventually decays the diffusion of nanoparticles toward the base wall. At maximum  $Da = 10^{-1}$ , the upper cell is stretched further laterally and greater expansion of isotherms is witnessed in the core region with the emergence of more yellow/orange (hotter) iso-concentrations. Therefore the distribution of the iso-concentrations in the enclosure enhances significantly as the Darcy number rises. Although permeability effects do not feature in the species diffusion “Eq. (15)” or the energy balance “Eq. (14)” directly, there is significant coupling between velocities, temperatures and concentrations via the thermo-solutal species buoyancy term in the secondary velocity “Eq. (13)” i.e.  $Ri(\theta - Nr \phi)$ . This results in a significant impact of Darcy number on both thermal and nanoparticle concentration fields in the regime. Transport characteristics are considerably modified via the presence of a porous material which can therefore be deployed to great effect in real fuel cell and materials fabrication operations for regulating flow and adjusting heat and mass diffusion.

Figures 4 (A-C) illustrate the streamlines, isotherms, and iso-concentrations contour plots for the impact of the Grashof number. The ratio of the buoyancy

force to the drag force is identified as  $Gr$ . Boosting the Grashof number values implies that the buoyancy forces dominate the viscous force, which results in an enhancement in thermal convection and the generation of stronger thermal convection currents in the enclosure regime. As seen in Fig. 4, for growing the Grashof number values, the flow field is dominant at the right wall compared with the left wall. A dual cell topology with two-cell sub-structure is computed at  $Gr = 10^2$ , and  $Gr = 10^3$ ; however, at  $Gr = 10^4$ , (maximum Grashof number), this merges into a single cell structure near the upper wall. Clearly, the intensification in thermal buoyancy leads to significant morphing in the streamline distributions which are always dominant in the vertical direction parallel to the vertical walls but become more intensified with a higher Grashof number. The characteristics of the isotherms and iso-concentrations are almost the same for  $Gr = 10^2$ , and  $Gr = 10^3$ , which indicates that there is no significant influence of Grashof number on the isotherms and iso-concentrations at lower Grashof number. However, a transition in the isotherms and iso-concentrations is induced at higher Grashof number  $Gr = 10^4$ . At  $Gr = 10^2$ , and  $Gr = 10^3$ , the isotherms are parallel to the upper and lower walls and sparsely distributed in the hottest (core) region with clear symmetry is observed. At  $Gr = 10^4$ , however strong (parabolic) distortion is induced near the upper wall which incurs into the core zone and distorts the profiles leading to more intense thermal diffusion in the core region. However, the base wall region remains undisturbed. With lower  $Gr$  values the iso-concentrations are again parallel at the upper and lower walls with a weak central zone which exhibits the absence of nanoparticle circulation. At maximum  $Gr$ , again significant warping of the iso-concentrations is computed near the upper wall which encroaches deeper into the core region, also inducing a slight distortion in the lower zone iso-concentrations (which eventually resume parallel distributions near the base wall); however, symmetry about the vertical centerline in the enclosure is still maintained. The Grashof number features in the Richardson number, which in turn arises in the coupling terms,  $Ri(\theta - Nr \phi)$  in the secondary momentum "Eq. (14)". This body force, therefore, has a very marked influence on the transport phenomena in the cavity.

The impact of buoyancy ratio parameter ( $Nr$ ) is illustrated in Figs. 5 (A-C). It is known that  $Nr = \frac{(C_h - C_c)(\rho_s - \rho_f)}{(1 - C_c)\rho_f(T_h - T_c)\beta_f}$  which expresses the ratio of nanoparticle species buoyancy force to thermal buoyancy force. The streamlines indicate that at the lower values of  $Nr$ , thermal buoyancy is dominated by species (solutal) buoyancy. However, as  $Nr$  attains the value 1, both buoyancy forces contribute eventually. This produces stronger natural convection, and the right vortex cell is strengthened. The isotherms also do not change substantially at lower  $Nr$  values. However, at higher values, the upper distorted zone pushes further into the core region and there is an expansion of the hot zone laterally. For the iso-concentrations, with  $Nr = 0.1$  and  $0.5$  (stronger species buoyancy force), the upper distorted zone and lower parallel zone with the intermediate absence of diffusion in the core zone, are depicted. The stronger intensity in iso-concentrations is observed at the upper

wall with weak distortion in the core region and then slightly warped distributions which evolve into a parallel distribution at the lower wall. However, the upper zone extends deeper into the core region when  $Nr = 0.5$  compared with  $Nr = 0.1$ . At  $Nr = 1$ , the incursion of the upper distorted cell structure is intensified and moves more strongly in a lateral sense in the core region. The streamlines and isotherms plots that when  $Nr = 1$ , the transport in the regime is significantly morphed. While species buoyancy does contribute, the dominant effect is thermal buoyancy (natural convection) which in all cases leads to a lateral intensification in the structures computed and encourages in particular, circulation near the hot wall. The computed patterns confirm the augmentation in heat transfer is achieved with stronger thermal buoyancy. The implication is that the regime behaviour is more sensitive to thermal buoyancy than species buoyancy and this can be exploited to great effect in the design of heat exchangers, fuel cells, etc<sup>54,56</sup>. Further, noticed that the species diffusion is raised by magnifying values of  $Nr$ .

The impact of Hartmann number ( $Ha$ ) is illustrated in Figs. 6 (A-C). It is known that the Hartmann number represents the impact of Lorentz's magnetic drag force on the viscous hydrodynamic force in the enclosure. For  $Ha > 1$ , as considered here, the magnetic drag force is dominant. This strongly increases the magnetic drag forces featured in both the momentum "Eq. (13) and (14)". It is observed that there is a significant interplay between the primary and secondary velocities due to these magnetic body forces. The streamline plots show that the two convective vertical cells are formed and they are enlarged with enhancing Hartmann number values. A stronger magnetic field clearly damps the flow and allows some growth of the vortex cells, especially towards the lower wall. The core of isotherms and iso-concentrations are weakly modified at higher values of the Hartmann number. The upper isotherms push deeper into the core zone indicating that temperatures are escalated with a higher magnetic field. This is due to the dissipation of kinetic energy as thermal energy from supplementary work expended in dragging the magnetized nanoliquid against the action of the oblique magnetic field. The central cell in the iso-concentration plots at lower  $Ha (= 15)$  value is eliminated with greater  $Ha (= 20, 25)$ . The upper distorted zone near the top wall encroaches deeper into the enclosure and the iso-concentrations values become more constricted near the lower wall. Mass (nanoparticle) diffusion is therefore encouraged with the stronger magnetic field.

The effect of the magnetic field inclination angle ( $\Phi$ ) is illustrated in Figs. 7 (A-C). The magnetic drag forces arising in both the momentum "Eq. (13) and (14)". As shown in Fig. 1, the magnetic field is inclined to the horizontal wall. When  $\Phi = \frac{\pi}{4}$ , the magnetic field is parallel to the base wall. When  $\Phi = \frac{\pi}{4}$ , it is inclined and when  $\Phi = \frac{\pi}{2}$ , it is parallel to the vertical wall. These three orientations span the range of important angles. When  $\Phi = 0$ , the magnetic forces reduce to 0 (in the primary velocity equation) and  $-\frac{Ha^2}{Re}V$  (in the secondary velocity equation),

since  $\sin 0 = 0$  and  $\cos 0 = 1$ . When  $\Phi = \frac{\pi}{2}$ , the magnetic force is only retained in the primary momentum equation since  $\sin \frac{\pi}{2} = 1$  and  $\cos \frac{\pi}{2} = 0$ . This magnetic force is  $-\frac{Ha^2}{Re}U$ . There is clearly a formation of two convective cells appearing in the enclosure and those convective cells are located close to the enclosure's top wall. The lower zone is unoccupied. The left circulating zone is denser compared with the right circulating zone. An augmentation in the magnetic field inclination angle does not cause any significant variation in the convective cells. The isotherms illustrate that the formed convective cells cause a boost in heat conduction towards the cold wall side. It is detected that the magnetic field inclination angle has a weak impact on isotherms since the convective cells are the same with only slight variations in the location of the core for larger values of inclination angle. When  $\Phi = 0$ , the iso-concentrations form a small circulation in the middle of the enclosure. Further, it is observed from the graph that the core of convective cells is moving towards the cold bottom wall side. Among the streamline, isotherm, and iso-concentration distributions, the magnifications in inclination angle values have marginally the highest influence on the iso-concentrations. The overall orientation of the magnetic field induces some relatively weak modifications in the transport phenomena in the enclosure.

Figures 8 (A-C) illustrate the impression of Richardson number ( $Ri$ ) on streamlines, isotherms, and iso-concentrations. It is to be noted that the Richardson number is the proportion of free convection to forced convection and it is expressed as  $Ri = \frac{Gr}{Re^2}$ . The values for Richardson number,  $Ri = 10^{-3}, 1, 10^2$  are chosen in order to characterize the forced convection, mixed convection, and free convection dominated modes of heat transmission. It is clear that the flow pattern of the left circulating cell is assertive compared with the right circulating cell. The double vortex cells are again vertically biased with two internal smaller circulation structures. The fluid flow, temperature, and concentration contours are relatively weakly affected by an augmentation in values of the Richardson number. Symmetry is sustained in the isotherms and iso-concentrations. The buoyancy ratio and in particular thermal buoyancy (studied earlier) has a more dramatic influence on internal circulation transport phenomena compared with Richardson number.

Figures 9 and 10 present the variation in  $Nu$  with various parameters. Figure 9 elucidates that the Grashof number increments diminish the local Nusselt number distribution i.e. the magnifications in the Grashof number values enhance thermal buoyancy which suppresses the rate of heat transmission at the boundary because bulk fluid is produced inside the cavity due to temperature enhancement. The local heat transfer rate profiles decrease with decreasing values of Darcy number as seen in Fig. 10. It is further noticed that a decrease in  $Da$  initially depletes  $Nu$  for low values of  $x$  coordinate, thereafter an upsurge is observed with subsequent elevation in the values of  $x$  coordinate. The variation magnitude of the Nusselt number is

high for lower Darcy number values compared with higher values of Darcy number.

#### 4. Conclusions

Motivated by simulating hybrid magneto-nanofluid fuel cells, a theoretical and numerical study on transport phenomena of mixed convective flow in a rectangular cavity saturated with a Darcian permeable medium and filled with an electrically conducting nanoliquid under the effect of oblique (inclined) static magnetic field, is presented. Buongiorno's two-component nanoscale model has been utilized to characterize the species diffusion, Brownian motion, and thermophoretic body force effects. The simulated enclosure has adiabatic walls and hot slits in the center of the vertical walls. The enclosure's base and upper horizontal walls are sustained at a uniformly cold temperature. The transformed non-dimension governing equations subject to the considered boundary conditions are worked out by utilizing the MAC technique. The effects of the key physical parameters on streamlines, isotherms, iso-concentrations contour plots, and local heat transmission rate are studied. The key observations are listed below:

- (1) The effect of the porous parameter is significant in the streamlines, isotherms, and iso-concentrations. Thus, the porous medium can significantly control the transport phenomena in the enclosure.
- (2) The variations in  $\Phi$ ,  $Ha$ , and  $Ri$  have a relatively weak effect on the transport phenomena of nanofluid flow in the rectangular enclosure.
- (3) The concentration, temperature, and velocity contours are strongly modified by the variations in the Grashof number (thermal buoyancy parameter).
- (4) An enhancement in  $Nr$  causes a magnification in temperature contours. Further, noticed that the  $Nr$  has a notable impact on flow and concentration contours.
- (5) A decay in Darcy number diminishes the local Nusselt number.
- (6) Local heat transmission rate decreases for higher values of  $Gr$ .

The MAC technique is shown to be a very appropriate numerical methodology for simulating nonlinear multi-physical enclosure nanoliquid flows of relevance to hybrid fuel cell and magnetic nanomaterials processing systems. The present study has however neglected the electromagnetic induction and specific nanoparticle<sup>56</sup>. These may be considered in future investigations.

#### Acknowledgment

The second author is thankful to the Ministry of Education, the United Arab Emirates for the financial assistance to complete this research work.

#### References

1. S. U. S. Choi, and J. A. Eastman, *Argonne National Lab. (ANL), Argonne, IL (United States)*, (1995).

- 28 A. Sumithra, V. R. Prasad, R. Sivaraj, Ho-Hon Leung, O. A. Bég & Firuz Kamalov, S. Kuharat, B. Rushi Kumar
2. A. Mostafazadeh, D. Toghraie, R. Mashayekhi, and O. A. Akbari, *J. Therm. Anal. Calorim.*, **1(138)**, pp. 779–794 (2019).
  3. H. Bazdar, D. Toghraie, F. Pourfattah, O. A. Akbari, H. M. Nguyen, and A. Asadi, *J. Therm. Anal. Calorim.*, **3(139)**, pp. 2365–2380 (2020).
  4. H. Laidoudi, A. Abderrahmane, A. M. Saeed, K. Guedri, O. Younis, R. Marzouki, and N. A. Shah, *Nanomaterials*, **12(14)**, pp. 2373, (2020).
  5. A. Jirawattanapanit, A. Abderrahmane, A. Mourad, K. Guedri, O. Younis, B. Bouallegue, and N. A. Shah, *Nanomaterials*, **12(15)**, pp. 2519 (2020).
  6. A. Sumithra, and R. Sivaraj, *Waves in Random Complex Media*, DOI: 10.1080/17455030.2022.2139014.
  7. A. Sumithra, and R. Sivaraj, *EPJ Plus*, **137(10)**, pp. 1193 (2022).
  8. N. A. Shah, A. Wakif, E. R. El-Zahar, S. Ahmad, and S. J. Yook, *Case Stud. Therm. Eng.*, pp. 102046 (2022).
  9. K. Sajjan, N.A. Shah, N.A. Ahammad, C.S.K. Raju, M.D. Kumar, and W. Weera, *AIMS Mathematics*, **7(10)**, pp. 18416–18449 (2022).
  10. R. Zhang, N.A. Ahammad, C.S.K. Raju, S.M. Upadhya, N.A. Shah, and S-J. Yook, *Int. Commun. Heat Mass Transf.*, **138**, pp. 106418 (2022).
  11. N. A. Shah, D. Vieru, and E. R. El-Zahar, *Waves in Random and Complex Media*, DOI: 10.1080/17455030.2022.2118392.
  12. GH. R. Kefayati, *Int. J. Heat Mass Transf.*, **94**, pp. 582–624 (2016).
  13. J. C. Umavathi, and O. A. Bég, *Microfluidics and Nanofluidics*, **25(6)**, pp. 1–20 (2021).
  14. A. M. Rashad, T. Armaghani, A. J. Chamkha, and M. A. Mansour, *Chinese J. Phys.*, **56(1)**, pp. 193–211 (2018).
  15. M. Aneja, A. Chandra, and S. Sharma, *Int. Commun. Heat Mass Transf.*, **114**, pp. 104555 (2020).
  16. G. Rasool, N.A. Shah, E.R. El-Zahar, and A. Wakif, *Waves Random Complex Media*, pp. 1-20 (2022).
  17. H. M. Elshehabe, and S. E. Ahmed, *Int. J. Heat Mass Transf.*, **88**, pp. 181–202 (2015).
  18. N. S. Gibanov, M. A. Sheremet, H. F. Oztop, and A. H. Nidal, *Int. J. Heat Mass Transf.*, **114**, pp. 1086–1097 (2017).
  19. B. M. D. H. Khan, V. R. Prasad, and R. B. Vijaya, *Nonlinear Engineering*, **7(4)**, pp. 253–261 (2018).
  20. C. C. Cho, *Int. J. Mech. Sci.*, **151**, pp. 703–714 (2019).
  21. S. Hussain, and S. E. Ahmed, *Int. J. Mech. Sci.*, **157**, pp. 692–702 (2019).
  22. N. H. Abu-Hamdeh, H. F. Oztop, and K. A. Alnefaie, *Alex. Eng. J.*, **59(3)**, pp.1735–1750 (2020).
  23. A. Rauf, N. A. Shah, A. Mushtaq, and T. Botmart, *AIMS Mathematics*, **8(1)**, pp. 164–193. doi:10.3934/math.2023008.
  24. F. Selimefendigil, H. F. ztop, and A. J. Chamkha, *J. Magn. Magn. Mater.*, **406**, pp. 266–281 (2016).
  25. N. S. Bondareva, and M. A. Sheremet, *J. Magn. Magn. Mater.*, **419**, pp. 476–484 (2016).
  26. K. Mehmood, S. Hussain, and M. Sagheer, *J. Mol. Liq.*, **238**, pp. 485–498 (2017).
  27. F. Selimefendigil, and H. F. ztop, *Physica A Stat. Mech. Appl.*, **540**, pp. 123004 (2020).
  28. M. A. Mansour, S. E. Ahmed, A. M. Aly, Z. A. S. Raizah, and Z. Morsy, *Chinese J. Phys.*, **68**, pp. 387–405 (2020).
  29. S. Hussain, M. Jamal, and B. P. Geridonmez, *Int. J. Therm. Sci.*, **161**, pp.106707

- (2021).
30. S. Eswaramoorthi, K. Loganathan, M. Faisal, T. Botmart, and N. A. Shah, *Ain Shams Engineering Journal*, Article ID 101887 (2022).
  31. J. Buongiorno, *ASME J. Heat Transfer*, **128**, pp. 240–250 (2006).
  32. M. A. Sheremet, and I. Pop, *Appl. Math. Comput.*, **266**, pp. 792–808 (2015).
  33. G. H. R. Kefayati, and N. A. C. Sidik, *Powder Technology*, **305**, pp. 679–703 (2017).
  34. G. Kumaran, O. D. Makinde, and R. Sivaraj, *Defect Diffus. Forum*, **387**, pp. 653–665 (2018).
  35. H. T. Basha, S. R. Gunakala, O. D. Makinde, and R. Sivaraj, *Defect Diffus. Forum*, **387**, pp. 343–351 (2018).
  36. L. Wang, X. Yang, C. Huang, Z. Chai, and B. Shi, *Appl. Therm. Eng.*, **146**, pp. 318–327 (2019).
  37. S. M. H. Zadeh, M. Sabour, S. Sazgara, and M. Ghalambaz, *Phys. A: Stat. Mech. Appl.*, **538**, pp. 122826 (2020).
  38. P. S. Reddy, and P. Sreedevi, *Chinese J. Phys.*, **72**, pp. 327–344 (2021).
  39. O. A. Bég, H. T. Basha, R. Sivaraj, and V. R. Prasad, *Int. J. Numer. Methods Heat Fluid*, **31(5)**, pp. 1475–1519 (2021).
  40. H. T. Basha, R. Sivaraj, A. S. Reddy, A. J. Chamkha, and M. Tilioua, *SN Appl. Sci.*, **2(3)**, pp. 1–14 (2020).
  41. H. T. Basha, and R. Sivaraj, *J. Appl. Comput. Mech.*, **8(2)**, pp. 566–579 (2020).
  42. J. Prakash, D. Tripathi, O. A. Bég, A. K. Tiwari, and R. Kumar, *Heat Transfer*, (2021).
  43. M. D. Shamshuddin, F. Mabood, and O. A. Bég, *Int. J. Simul. Model.*, pp. 1–15 (2021).
  44. J. C. Umavathi, S. L. Patil, B. Mahanthesh, and O. A. Bég, *SAGE Publications Sage UK: London, England*, **235(3-4)**, pp. 67–81 (2021).
  45. O. A. Bég, K. Venkatadri, V. R. Prasad, T. A. Beg, A. Kadir, and J. C. Henry, *Mater. Sci. Eng. B.*, **261**, pp. 114722 (2020).
  46. O. A. Bég, K. Venkatadri, V. R. Prasad, T. A. Bég, and H. J. Leonard, *Proc. IMechE-Part C-J. Mechanical Engineering Science*, (2021).
  47. M. K. Abdolbaqi, W. H. Azmi, R. Mamat, K. V. Sharma, and G. Najafi, *Appl. Therm. Eng.*, **102**, pp. 932–941 (2016).
  48. V. Amati, E. Sciubba, and C. Toro, *ASME International Mechanical Engineering Congress and Exposition*, **48692**, pp. 721–731 (2008).
  49. J. Albadr, S. Tayal, and M. Alasadi, *Case Stud. Therm. Eng.*, **1(1)**, pp. 38–44 (2013).
  50. R. Islam, *RMIT University*, (2016).
  51. A. Pantokratoras, *Journal of Heat Transfer*, **114(11)**, pp. 115501 (2022).
  52. J. Bouchard, A. Cayla, E. Devaux, and C. Campagne, *Compos Sci Technol.*, **86**, pp. 177–184 (2013).
  53. C. Wan, B.S.V. Patnaik, and D.G.W. Wei, *Numer. Heat Transf. B: Fundam.*, **40(3)**, pp. 199228 (2001).
  54. G. H. R. Kefayati, *Int. J. Heat Mass Transf.*, **112**, pp. 709–744 (2017).
  55. T.S. Devi, C.V. Lakshmi, K. Venkatadri, V.R. Prasad, O.A. Beg, and M.S. Reddy, *Heat Transf.*, **49(4)**, pp. 17691787 (2020).
  56. O. A. Bég, S. Kuharat, M. Ferdows, M. Das, A. Kadir, and M. D. Shamshuddin, *Proceedings of the Institution of Mechanical Engineers, Part N: Journal of Nanomaterials, Nanoengineering and Nanosystems*, **233(1)**, pp. 27–45 (2019).